

**Detailed instantaneous ionization rate of  $H_2^+$  in an intense laser field**Mohsen Vafae, <sup>1,\*</sup> Hassan Sabzyan, <sup>1,†</sup> Zahra Vafae, <sup>2</sup> and Ali Katanforoush <sup>3</sup><sup>1</sup>*Department of Chemistry, University of Isfahan, Isfahan 81746-73441, I. R. Iran*<sup>2</sup>*Department of Mathematics, University of Isfahan, Isfahan 81746-73441, I. R. Iran*<sup>3</sup>*School of Mathematics, Institute for Studies in Theoretical Physics and Mathematics (IPM), Tehran 19395-5746, I. R. Iran*

(Received 10 June 2006; published 23 October 2006)

Component instantaneous ionization rate (IIR) is introduced and the approach of its calculation is formulated. The component IIR's and the overall (time-averaged) component ionization rates are calculated for  $H_2^+$  at different values of internuclear distance in a linearly polarized laser field with  $I=1.0 \times 10^{14}$  W/cm<sup>2</sup> intensity and  $\lambda=1064$  nm wavelength by direct numerical solution of the fixed-nuclei full dimensional time-dependent Schrödinger equation. The exact overall component ionization rates calculated by time-averaging of the component IIR are compared with those calculated approximately via the virtual detector (VD) method. Details of the time-dependent behavior of the outgoing and incoming electron wave packets of the  $H_2^+$  system in intense laser field at subfemtosecond time scale are studied based on the calculated component IIR. It is shown clearly that the positive (outgoing electron wave packet) signals of the IIR and its  $z$  component are strong and sharp but the negative (returning electron wave packet) signals of the IIR are smooth and weak. The structure of the  $\rho$  component of the IIR has smooth structure. Relation between the  $R$ -dependent ionization rate and duration of the ramp of the laser pulse is studied and it is explicitly shown that for internuclear distance  $R < 5.6$ , when the laser pulse is turned on without a ramp, the first peak of  $R$ -dependent ionization rates moves towards the peak of the lower time-dependent Floquet quasienergy state (QES).

DOI: [10.1103/PhysRevA.74.043416](https://doi.org/10.1103/PhysRevA.74.043416)

PACS number(s): 33.80.Rv, 42.50.Hz, 42.65.Ky

**I. INTRODUCTION**

In an intense laser field, atoms and molecules are ionized in attosecond time scales [1]. In addition to the electronic dynamics, molecules have nuclear dynamics, vibration, and rotation in femtosecond and picosecond time scales. Extensive studies carried out experimentally and theoretically on the  $H_2$  and  $H_2^+$  systems have revealed comprehensive new phenomena [2–4]. Studies of the dynamics of these two systems exposed to an intense laser field are very complicated because two processes, ionization and dissociation, are involved simultaneously.

An interesting and complicated effect observed experimentally and theoretically is the enhancement of the ionization rate of  $H_2^+$  as a function of H-H internuclear separation that results in maxima at some critical points. Indirect [5,6] and direct [7] evidence has been reported for a similar behavior in more complex molecules. In order to characterize and interpret the observed enhanced ionization rates [8–13], recent theoretical studies on the  $H_2^+$  laser interaction have concentrated on the calculation of the ionization rate as a function of internuclear distance  $R$  [14–28]. The enhanced ionization has a very important role in the interpretation of the intramolecular dynamics and fragmentation in an intense laser field [24].

Recently, calculations of the ionization rates have had very important improvements. For the Ti:sapphire laser at intensities starting from just above the Coulomb explosion (CE) threshold, it is shown that the  $R$ -dependent ionization peaks move towards small internuclear distances, and their

structures become simpler and smoother with the increase in the intensity of the laser pulse (i.e., with the decrease in the Keldysh parameter) [22]. The virtual detector method made it possible to define and distinguish ionization rates and outgoing norms from different boundaries, which can be used to study details of the dynamics of the spatial evolution of the electron wave function [18]. Moreover, based on the instantaneous ionization rates (IIR's), details of the time-dependent behavior of the system following the variations of the laser field can be extracted and used in the interpretation of the enhanced ionization rates [28]. This approach allows us to determine not only the instantaneous intensity but also the instantaneous direction of the electronic current. This approach provides direct evidence for the existence of the effect of charge-resonance-enhanced multiphoton resonances of the quasienergy states (QES) with excited electronic states at some particular internuclear distances [19,28].

In this article, components of the instantaneous ionization rate are introduced and the approach of their calculations is formulated. The component IIR's and the overall (time-averaged) component ionization rates are calculated for  $H_2^+$  at different values of internuclear distance in a linearly polarized laser field with  $I=1.0 \times 10^{14}$  W/cm<sup>2</sup> intensity and  $\lambda=1064$  nm wavelength by direct numerical solution of the fixed-nuclei full dimensional time-dependent Schrödinger equation (TDSE). The calculated overall component ionization rates calculated in this approach are compared with the results of the virtual detector (VD) method [18]. The relation between the  $R$ -dependent ionization rate and duration of the ramp of the laser pulse is studied and compared with the results obtained by time-dependent Floquet calculations [19]. And finally, details of the dynamics of the electron wave packets of the  $H_2^+$  system in an intense laser field based on the calculated components of IIR are studied.

\*Electronic address: [MohsenVafae@sci.ui.ac.ir](mailto:MohsenVafae@sci.ui.ac.ir)†Electronic address: [sabzyan@sci.ui.ac.ir](mailto:sabzyan@sci.ui.ac.ir)

## II. COMPONENTS OF THE INSTANTANEOUS IONIZATION RATE

The instantaneous energy of a system in an intense laser field can be decomposed and calculated as  $E(t) = E_{\text{Re}} + iE_{\text{Im}}$  [28], where  $E_{\text{Re}}$  and  $E_{\text{Im}}$  are the real and imaginary parts of the total electronic energy, respectively. The instantaneous ionization rate (IIR) denoted by  $\Gamma(t)$  is defined as [28]

$$\Gamma(t) = \frac{-2E_{\text{Im}}(t)}{N(t)}. \quad (1)$$

The imaginary energy can be decomposed in a cylindrical coordinate as  $E_{\text{Im}} = T_{\text{Im},z} + T_{\text{Im},\rho}$ ; the potential part of the imaginary energy,  $V_{\text{Im}}$ , is zero and thus has no contribution to  $E_{\text{Im}}$ . Therefore, Eq. (1) can be rewritten as

$$\Gamma(t) = \frac{-2T_{\text{Im},z}(t)}{N(t)} + \frac{-2T_{\text{Im},\rho}(t)}{N(t)} = \Gamma_z(t) + \Gamma_\rho(t). \quad (2)$$

This equation shows that the total IIR,  $\Gamma(t)$ , can be decomposed into its two  $z$  and  $\rho$  IIR components,  $\Gamma_z(t)$  and  $\Gamma_\rho(t)$ . This relation, Eq. (2), defines component instantaneous ionization rates and their relation with the total IIR.

The ionization rate,  $\Gamma(t)$ , can also be obtained by calculating the time-dependent norm,  $N(t)$ , of the wave function via

$$\Gamma(t) = \frac{-d \ln[N(t)/N(0)]}{dt}, \quad (3)$$

where  $N(t) = \|\Psi(t)\|^2$  and  $N(0) = \|\Psi(0)\|^2$  is the initial value of the norm. We have shown already [18] that in a cylindrical coordinate, it is possible to decompose the outgoing norm of the system as  $N_{\text{VD}}^O(t) = N_z^O(t) + N_\rho^O(t)$ , in which  $N_z^O(t)$  and  $N_\rho^O(t)$  are respectively the instantaneous outgoing norms from the  $z$  and  $\rho$  boundaries, so that the overall ionization rate  $\Gamma_{\text{VD}}$  and its  $z$  and  $\rho$  components,  $\Gamma_z$  and  $\Gamma_\rho$ , calculated via the virtual detector (VD) method, are connected via [18]

$$\Gamma_{\text{VD}} \approx \Gamma_z + \Gamma_\rho. \quad (4)$$

This means that the total VD ionization rate  $\Gamma_{\text{VD}}$  is approximately equal to the sum of the component ionization rates for the  $z$  and  $\rho$  boundaries  $\Gamma_z$  and  $\Gamma_\rho$ , both calculated via the VD method. While the equality of Eq. (4) is an approximation, Eq. (2) is exact.

## III. NUMERICAL SOLUTION OF THE TDSE

The component IIR's and the overall component ionization rates obtained via the approach introduced in this work, Eqs. (1) and (2), or via the VD method, Eq. (4), for different values of internuclear distance can be numerically calculated for  $\text{H}_2^+$  in a linearly polarized laser field with  $1.0 \times 10^{14}$  W/cm<sup>2</sup> intensity and  $\lambda = 1064$  nm wavelength by direct solution of the fixed-nuclei full dimensional time-dependent Schrödinger equation. The time-dependent Schrödinger equation, in the cylindrical polar coordinates for the  $\text{H}_2^+$  molecular ion exposed to the laser field of  $E(t) = E_0 f(t) \cos(\omega t)$  applied along the internuclear axis ( $z$  axis) in atomic units, reads as [16,18]

$$i \frac{\partial \psi(z, \rho, t)}{\partial t} = H(z, \rho, t) \psi(z, \rho, t), \quad (5)$$

in which

$$H(z, \rho, t) = -\frac{2m_p + m_e}{4m_p m_e} \left[ \frac{\partial^2}{\partial \rho^2} + \frac{1}{\rho} \frac{\partial}{\partial \rho} + \frac{\partial^2}{\partial z^2} \right] + V_C(z, \rho, t), \quad (6)$$

$$V_C(z, \rho, t) = -\sum_{\pm} [(z \pm R/2)^2 + \rho^2]^{-1/2} + \left( \frac{2m_p + 2m_e}{2m_p + m_e} \right) z E_0 f(t) \cos(\omega t). \quad (7)$$

The laser pulse envelope  $f(t)$  is set as

$$f(t) = \begin{cases} \frac{1}{2} \left[ 1 - \cos\left(\frac{\pi t}{\tau_1}\right) \right] & \text{for } 0 \leq t \leq \tau_1, \\ 1 & \text{for } \tau_1 \leq t \leq \tau_1 + \tau_2, \\ \frac{1}{2} \left[ 1 - \cos\left(\frac{\pi(t - \tau_2 - 2\tau_1)}{\tau_1}\right) \right] & \text{for } \tau_1 + \tau_2 \leq t \leq 2\tau_1 + \tau_2, \\ 0 & \text{for } 2\tau_1 + \tau_2 \leq t, \end{cases} \quad (8)$$

with  $\tau_1$  and  $\tau_2$  being the rising time and duration of the laser pulse at its full-scale amplitude, respectively. The differential operators are discretized by the 11-point difference formulas which have tenth-order accuracies [28]. More details of our calculations are described in our previous reports [18,28].

## IV. THE OVERALL IONIZATION RATES AND THEIR COMPONENTS

Simulation of the time-dependent behavior of the  $\text{H}_2^+$  system at some fixed internuclear separations in a box of (640, 170) size for the  $(z, \rho)$  coordinates carried out by direct solution of the TDSE in the presence of the linearly polarized

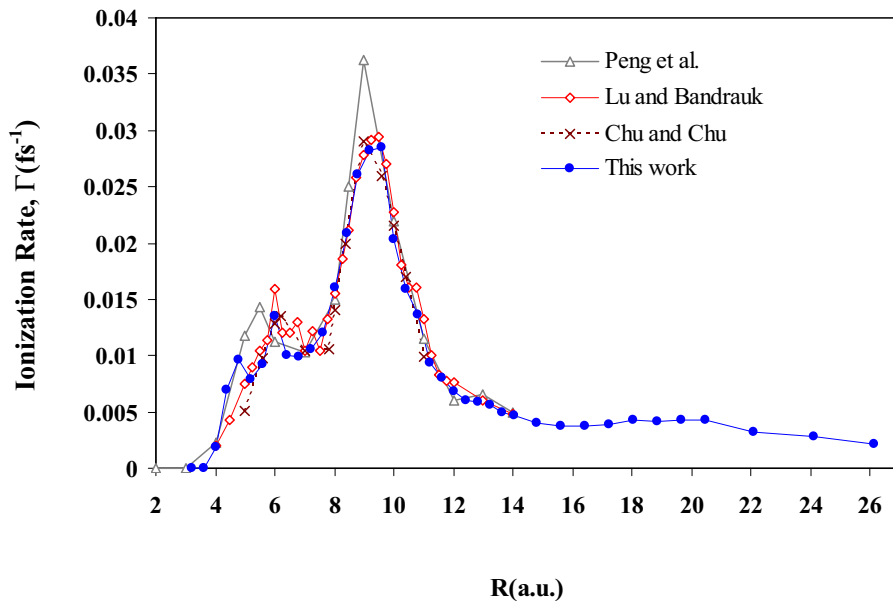


FIG. 1. (Color online) The ionization rate,  $\Gamma$ , of  $H_2^+$  in the linearly polarized laser field of  $I = 1.0 \times 10^{14} \text{ W/cm}^2$  intensity and  $\lambda = 1064 \text{ nm}$  wavelength, averaged from  $\tau = 10$  to  $\tau = 20$  cycles, as a function of  $R$  calculated in this series of research (●) [28] compared with the calculated ionization rates reported by Lu and Bandrauk ( $\Delta$ ) [16], Peng *et al.* ( $\square$ ) [17], and Chu and Chu ( $\times$ ) [19]. The isolated single point on the vertical coordinate at  $R = 27$  corresponds to the ionization rate of an isolated H atom.

laser field with  $I = 1.0 \times 10^{14} \text{ W/cm}^2$  intensity and  $\lambda = 1064 \text{ nm}$  wavelength (with  $\tau_1 = 5$  and  $\tau_2 = 15$ ) has been reported in our previous report [28]. Figure 1 shows the  $R$ -dependent ionization rates calculated for the  $H_2^+$  system (●). The overall ionization rate of  $H_2^+$  at each internuclear distance is calculated by averaging the calculated instantaneous ionization rates over the time period from  $\tau = 10$  to  $\tau = 20$  cycles of the laser field using Eq. (1) or (3). In addition to the results reported in our previous paper [28], this figure contains a set of points at large values of  $R$ , above 14.0. The isolated single point on the right vertical axis corresponding to the ionization rate of an isolated H atom in the same laser field is given for comparison. Figure 1 shows that after a fast and monotonic decrease at intermediate values of  $R$ , the ionization rates of  $H_2^+$  at large internuclear distances oscillate around the ionization rate of the isolated H atom. It has al-

ready been discussed that the calculated ionization rates, especially above  $R > 9.5$ , are in good agreement with those reported by other researchers [16,17,19]. Furthermore, the  $\Gamma$  versus  $R$  curve obtained in our studies has a fine structure with narrow and weak peaks below  $R = 6.5$ .

The IIR and its components for  $H_2^+$  at some fixed internuclear separations have been calculated by direct solution of the TDSE in the presence of the linearly polarized laser field with  $I = 1.0 \times 10^{14} \text{ W/cm}^2$  intensity and  $\lambda = 1064 \text{ nm}$  wavelength with the envelope parameters  $\tau_1 = 5$  and  $\tau_2 = 15$ . The overall ionization rate of  $H_2^+$  and the components of ionization rate at each internuclear distance is calculated by averaging the calculated IIR and its components over the period  $\tau = 10$  to  $\tau = 20$  using Eq. (2). Figure 2 shows the  $R$ -dependent total ionization rate  $\Gamma$  (●) and its components,

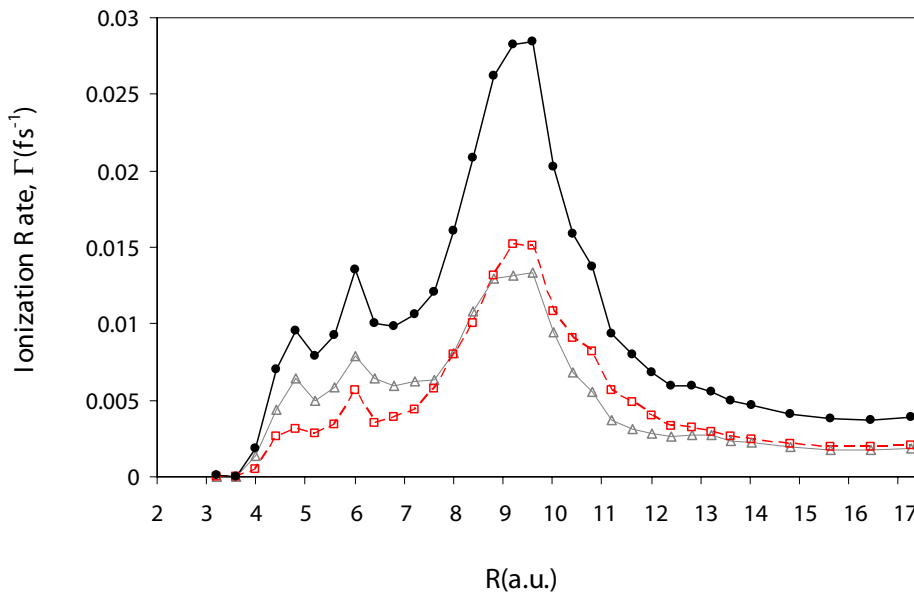


FIG. 2. (Color online)  $R$ -dependent total,  $\Gamma$  (●), and component,  $\Gamma_z$  ( $\Delta$ ) and  $\Gamma_\rho$  ( $\square$ ), ionization rates of the  $H_2^+$  system averaged from  $\tau = 10$  to  $\tau = 20$  cycles of the linearly polarized laser field of  $I = 1 \times 10^{14} \text{ W/cm}^2$  intensity and  $\lambda = 1064 \text{ nm}$  wavelength with the envelope parameters  $\tau_1 = 5$  and  $\tau_2 = 15$ , calculated in the present study using Eq. (2).

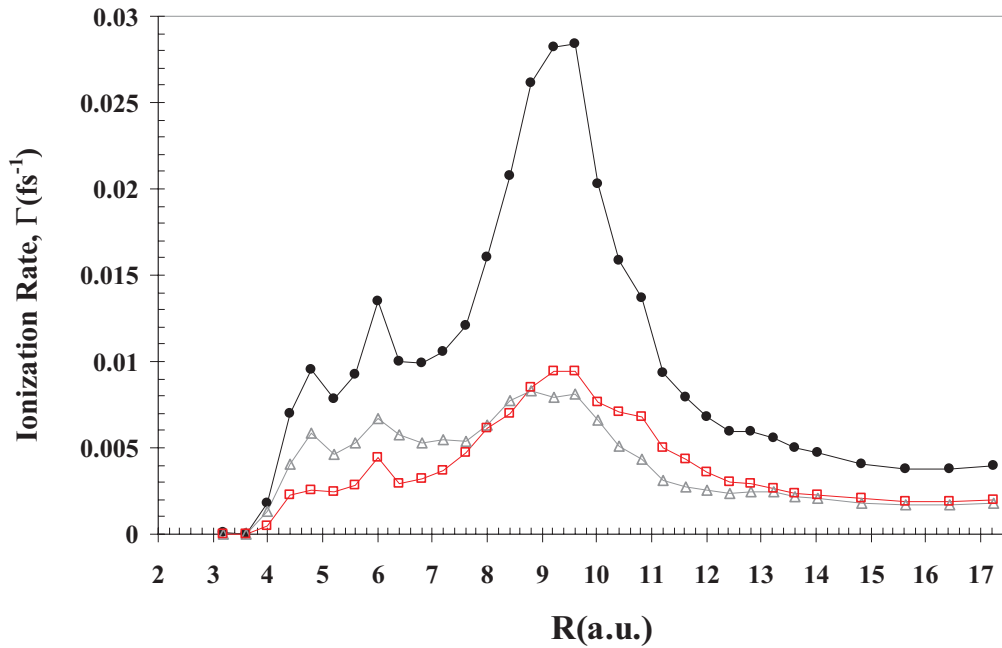


FIG. 3. (Color online) Calculated ionization rates of  $H_2^+$  in the linearly polarized laser field of  $I=1 \times 10^{14}$  W/cm<sup>2</sup> intensity and  $\lambda=1064$  nm wavelength using virtual detector (VD) method; the total VD ionization rate,  $\Gamma_{VD}$  ( $\bullet$ ), and its component ionization rates,  $\Gamma_z$  ( $\Delta$ ) and  $\Gamma_\rho$  ( $\square$ ). Compare this figure with Fig. 2.

$\Gamma_z$  ( $\Delta$ ) and  $\Gamma_\rho$  ( $\square$ ), calculated in the present study for the  $H_2^+$  system.

Figure 3 shows the corresponding total VD ionization rate,  $\Gamma_{VD}$  ( $\bullet$ ), and its components,  $\Gamma_z$  ( $\Delta$ ) and  $\Gamma_\rho$  ( $\square$ ) as functions of internuclear separation  $R$  calculated for  $H_2^+$  under the same conditions using Eq. (4). Structures of these  $R$ -dependent curves are similar to those of the corresponding curves in Fig. 2. While additivity of the VD ionization rate components  $\Gamma_z$  and  $\Gamma_\rho$ , and thus the equality of Eq. (4), is an approximation, the relation between the instantaneous ionization rate  $\Gamma(t)$  and its two components  $\Gamma_z(t)$  and  $\Gamma_\rho(t)$  in Eq. (2) is exact.

Comparison of Fig. 3 and Fig. 4(a) of Ref. [18] shows the wavelength effects of the intense laser field on the total VD ionization rate  $\Gamma_{VD}$  and its component ionization rates  $\Gamma_z$  and  $\Gamma_\rho$ . Variations of the component ionization rates are decreased with the increase in the wavelength from 790 nm to 1064 nm.

We can see from Fig. 2 that the first peak of the ionization rate at  $R \sim 4.8$  is mainly due to the  $z$ -coordinate ionization rate  $\Gamma_z$ , while the second and the third peaks, at 6.0 and 9.4, have contributions from both component ionization rates  $\Gamma_z$  and  $\Gamma_\rho$ ; comparative contributions of the component ionization rates for the two peaks are respectively  $\Gamma_z > \Gamma_\rho$  and  $\Gamma_\rho > \Gamma_z$ . In this simulation box, for internuclear distances above  $R=13.0$ , the two component ionization rates approach one another. As shown in our recent study [18], the relative magnitudes of the component ionization rates  $\Gamma_z$  and  $\Gamma_\rho$  depend also on the relative sizes of the simulation box along the  $\rho$  and  $z$  coordinates.

## V. THE IIR'S AND THEIR COMPONENTS

On the basis of Eqs. (1) and (2), for  $\Gamma(t)$  and its components  $\Gamma_z(t)$  and  $\Gamma_\rho(t)$ , positive (negative) values of instantaneous imaginary energy result in negative (positive) value for instantaneous ionization rates, and therefore, the positive (negative) values of the instantaneous imaginary energy correspond to the incoming (outgoing) of the electron to (from) the system [28].

The distinct advantage of the evaluation of the IIR via Eqs. (1) and (2) is that it makes it possible to follow the time-dependent ionization processes of a system and to study details of the ionization mechanism [28]. To show this ability more clearly, the time-dependent ionization rates of  $H_2^+$  in the linearly polarized field of  $I=1.0 \times 10^{14}$  W/cm<sup>2</sup> intensity and  $\lambda=1064$  nm wavelength for a number of selected internuclear separations have been calculated and presented in Fig. 4 that demonstrates the calculated IIR's (blue solid line) and their  $z$  (gray solid line) and  $\rho$  (red dotted line) components. The  $R$  values in Fig. 4 correspond to the peaks of the  $R$ -dependent ionization rates presented in Fig. 1, i.e., 4.8, 6.0, and 9.6. Figure 4 demonstrates the behavior of the IIR and its components over the two cycles (from  $\tau=14$  to  $\tau=16$ ) of the laser pulse (1 cycle  $\sim 3.55$  fs).

Analysis of Fig. 4 reveals that the overall pattern and structure of the IIR  $\Gamma(t)$  is dominantly determined by the  $z$  component IIR,  $\Gamma_z(t)$ . Figure 4 shows also that during one cycle of the laser pulse, the  $\Gamma_z(t)$  curves strongly fluctuate besides having a baseline consisting of an ordered oscillation with the same frequency as that of the laser field. Therefore, the sharp peaks of  $\Gamma(t)$  can primarily be attributed to the

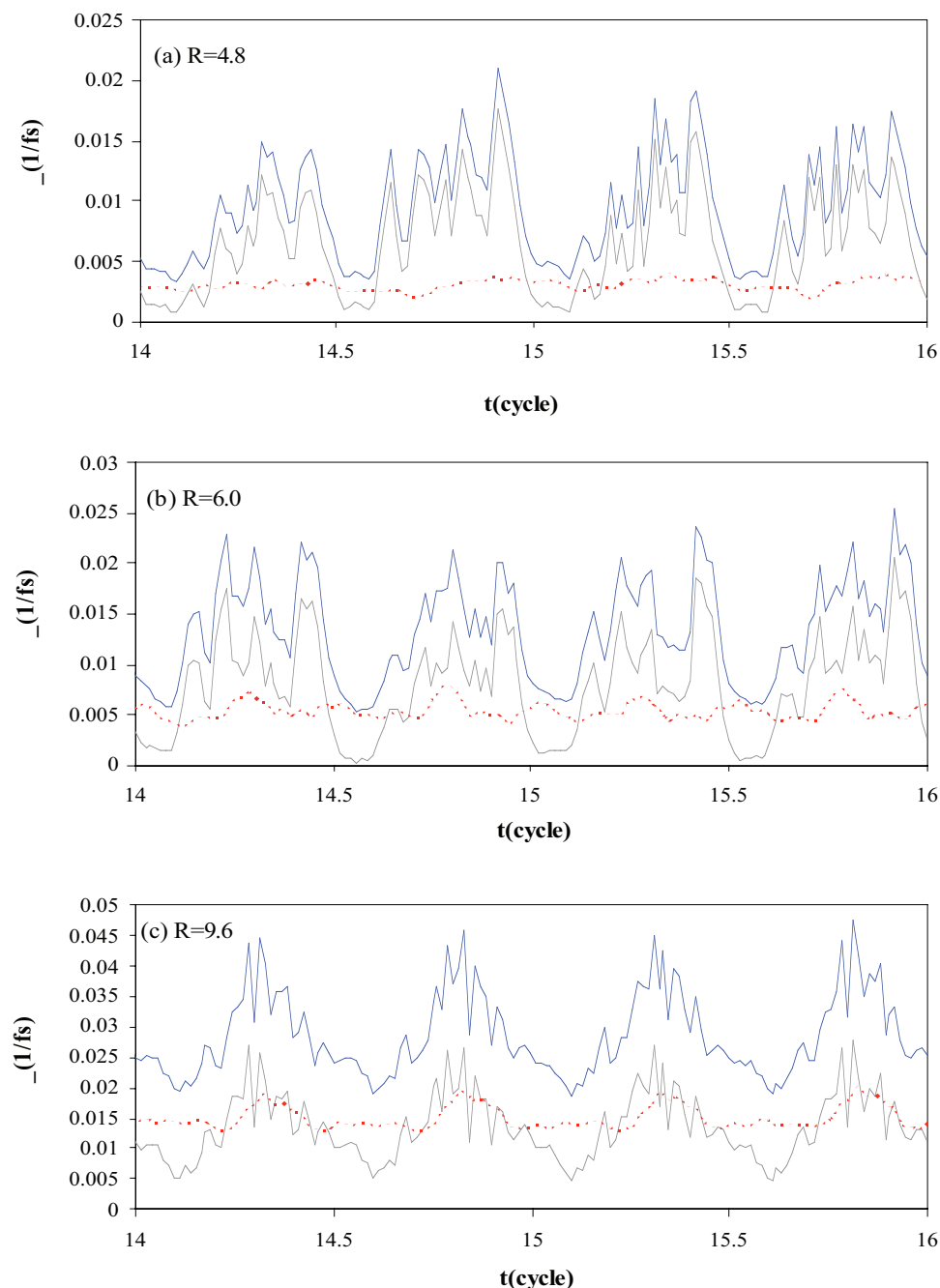


FIG. 4. (Color online) The instantaneous ionization rates of  $\text{H}_2^+$  in the linearly polarized laser field of  $I=1.0 \times 10^{14}$   $\text{W}/\text{cm}^2$  intensity and  $\lambda=1064$  nm wavelength over the two cycles, from  $\tau_1=14.0$  to  $\tau_2=16.0$ , of the laser pulse with the envelope parameters  $\tau_1=5$  and  $\tau_2=15$ . The IIR's (blue solid line) and their  $z$  (gray solid line) and  $\rho$  (red dotted line) components correspond to the peaks of the  $R$ -dependent ionization rates presented in Fig. 1, i.e., 4.8, 6.0, and 9.6.

variation of  $\Gamma_z(t)$ . In contrast to the variation of  $\Gamma_z(t)$ , variation of  $\Gamma_\rho(t)$  has a considerably smaller amplitude. Comparison between the two component ionization curves shows that variation of the outflow of electron from the  $\rho$  boundary is relatively much smoother than that from the  $z$  boundary. Each baseline peak of the  $\Gamma_z(t)$  IIR corresponds to one cycle of the laser pulse. The  $\Gamma_\rho(t)$  IIR curves do not show any significant oscillating structure, but have distinct smooth peaks for every half-cycle of the laser pulse. A general character of the baseline peaks of the  $\Gamma_\rho(t)$  is that [unlike those of the  $\Gamma_z(t)$ ] they do not fall to zero suddenly. Furthermore, the baseline peaks of the  $\Gamma_\rho(t)$  have significant intensity at  $R=9.4$ . Figure 4 shows clearly the details of the comparative trends of the two component IIR's demonstrated in Fig. 2 and discussed above.

## VI. EFFECT OF THE LASER PULSE RISING TIME ON THE $R$ -DEPENDENT IONIZATION RATES

Details of the enhanced ionization rates obtained based on the IIR gave direct evidence of the charge-resonance-enhanced multiphoton resonances of the quasienergy states (QES) with excited electronic states at some particular internuclear distances [28]. Here in this article, we present the effect of rising time of the laser pulse on the  $R$ -dependent ionization rates and will study details of the contributions of the individual time-dependent Floquet QES to the overall ionization rates.

To evaluate effect of the laser pulse rising time and to study individual contributions from the lower and upper sets of QES's to the overall ionization rates, we have reported in Fig. 5 the calculated overall ionization rates for different

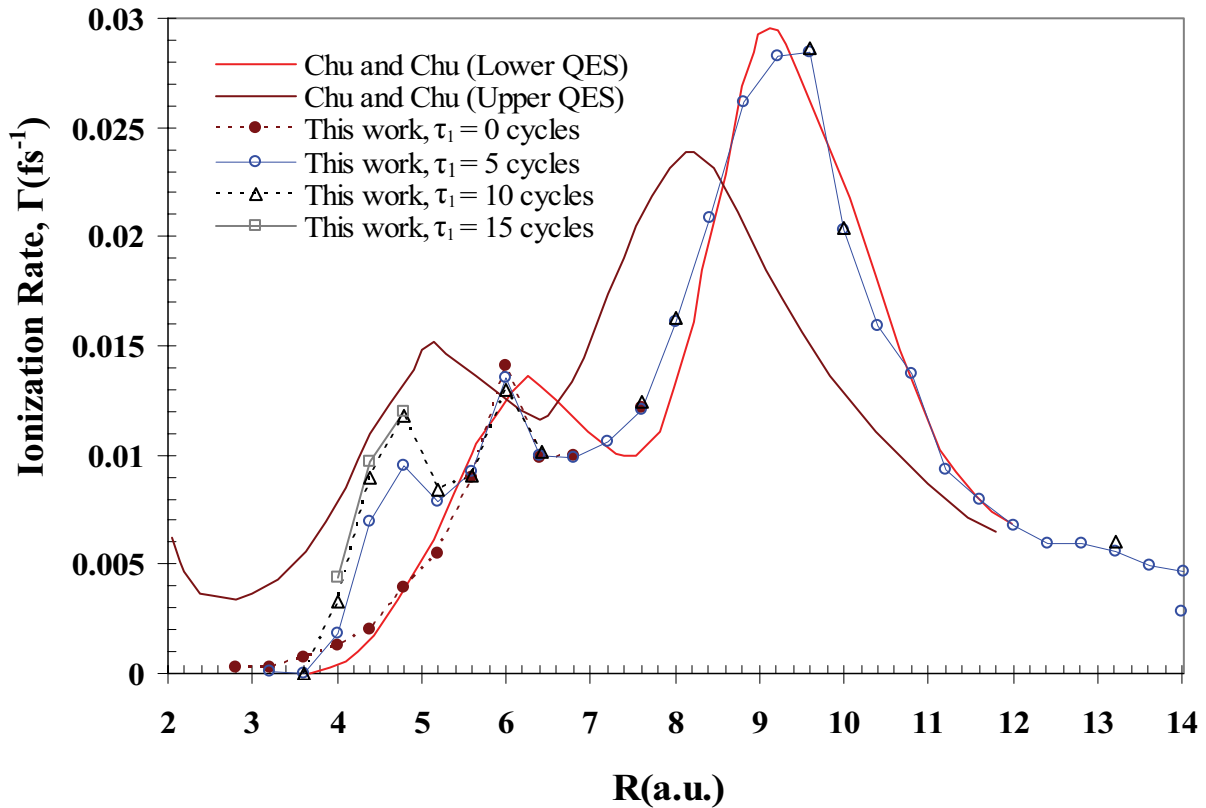


FIG. 5. (Color online) A comparison between the overall ionization rates for different rising times of the laser pulse,  $\tau_1$ , obtained in this work; the laser field are turned on with a ramp having a length of  $\tau_1 = 0$  ( $\bullet$ ),  $\tau_1 = 5$  ( $\circ$ ),  $\tau_1 = 10$  ( $\triangle$ ), and  $\tau_1 = 15$  ( $\square$ ) cycles, respectively. The individual contributions of the upper and lower quasienergy states (QES's) reported by Chu and Chu [19] are plotted for comparison.

laser pulses with different values of rising time  $\tau_1$ , and compared them with the isolated ionization rates of these two QES's reported by Chu and Chu [19]. As Fig. 5 shows, when the field is turned on with  $\tau_1 = 5$  cycles ( $\circ$ ), the ionization rates show three peaks, at 4.8, 6.0, and  $\sim 9.6$ . The peaks at 6.0 and 9.6 can be attributed to the peaks of the lower QES. But the first peak at 4.8 is placed between the peaks of the lower and upper QES. When the laser pulse is turned on immediately, i.e., with  $\tau_1 = 0$ , the calculated ionization rates derived by TDSE ( $\bullet$ ) correspond to those of the lower QES for  $R > 4.8$ . Figure 5 shows that the TDSE results for  $R < 4.8$  with  $\tau_1 = 0$  ( $\bullet$ ) take a small distance from the lower QES Floquet curve. This small difference is probably due to the avoided crossing of the upper and lower QES's. On the other hand, when the laser pulse is turned on with a ramp or rising part, with increasing  $\tau_1$  from zero to  $\tau_1 = 5$  ( $\circ$ ),  $\tau_1 = 10$  ( $\triangle$ ), and  $\tau_1 = 15$  ( $\square$ ) cycles, for example, the points of the ionization rates for  $R < 5.6$  approach the curve of the upper QES. We can conclude for H-H distance  $R < 5.6$  that when the laser pulse is turned on without a ramp, the first peak of the  $R$ -dependent ionization rates disappears and when the laser pulse is turned on with an initial ramp, both lower and upper QES's contribute to construct the first peak of the ionization rates at  $R = 4.8$ . For all of the  $R < 3.6$  and  $R > 5.2$  ranges, the ionization rates are determined by the lower QES and the amount of  $\tau_1$  does not have significant effect on the  $R$ -dependent ionization rate. Therefore, the pulse envelope determines contributions of different QES's to the overall ionization rate.

## VII. THE SPACE-TIME STRUCTURE OF THE INSTANTANEOUS ELECTRON WAVE PACKET

As mentioned in the preceding section, positive (negative) value of the instantaneous imaginary energy results in negative (positive) value for IIR, and therefore, the positive (negative) value of the instantaneous imaginary energy corresponds to the incoming (outgoing) of the electron to (from) the system. Designing a simulation to show both negative and positive IIR's is a difficult task, because the outgoing and incoming electron wave packets occur simultaneously and are summed to give the overall IIR. Moreover, almost usually the intensity of the positive IIR overcomes that of the negative IIR. Therefore, it seems that it is experimentally impossible to probe the negative IIR. So far, the negative ionization rate has not been reported or noticed in theoretical and computational works. In this section, we introduce details and structures of both negative and positive IIR's and their contributions to the corresponding component and total IIR's and their averages, and their effect on the  $R$ -dependent behavior of the ionization rates.

Calculations of the IIR of  $\text{H}_2^+$  at  $R = 9.6$  over the first five cycles of the linearly polarized laser field of  $I = 1.0 \times 10^{14}$  W/cm<sup>2</sup> and  $\lambda = 1064$  nm are repeated but with a pulse shape that is turned on as  $E_0 \cos(\omega t)$ , i.e., with  $\tau_1 = 0$ . These calculations of the (instantaneous) ionization rates were carried out for boxes all with (640, 170) size for the  $(z, \rho)$  co-

ordinates, shown in Fig. 6. Borders of the simulation box are placed such that  $-300 \leq z \leq 300$  and  $0 \leq \rho \leq 150$  and the absorber regions, the hatched area, are set at  $-320 \leq z \leq -300$  and  $300 \leq z \leq 320$  for the  $z$  and at  $150 \leq \rho \leq 170$  for the  $\rho$  coordinate [28]. The IIR's are calculated for the simulation boxes shown in Fig. 6 based on the electron wave packets passing the borders of the gray regions. In the present calculations of the IIR's, the same simulation boxes are used with different positions of the borders of the gray region which are set respectively at Figs. 6(a)  $-300 \leq z \leq 50$ , 6(b)  $-300 \leq z \leq 50$ , 6(c)  $-300 \leq z \leq 300$ , and 6(d)  $-250 \leq z \leq 250$  for the  $z$ , and  $0 \leq \rho \leq 150$  for the  $\rho$  coordinate, and finally at Fig. 6(e)  $-300 \leq z \leq 300$  for the  $z$  and  $0 \leq \rho \leq 100$  for the  $\rho$  coordinate. The two (red) bullets near the origin are the H nuclei having a 9.6 distance. Figure 7 demonstrates the calculated IIR's (blue line) and their  $z$  (gray line) and  $\rho$  (red line) components corresponding to the simulation boxes of Fig. 6.

Let us now study the IIR for the first simulation box [shown in Fig. 6(a)]. When the laser field is turned on, the electron wave packet starts out going from the gray region by passing through the  $z$  borders placed at  $-50$  and  $50$  and through the  $\rho$  border placed at  $150$ . Since the  $z$  borders are closer to the concentrated part (center) of the unperturbed ( $t=0$ ) electron wave packet, we thus expect to detect first the outgoing wave packet from the  $z$  borders much earlier than that from the  $\rho$  border. If one of the borders of the gray region is placed closer to (farther from) the nuclei (i.e., the center of the unperturbed wave packet), intensity of the outgoing wave packet from that border in the initial stages of the laser pulse becomes also stronger (weaker). Therefore, the outgoing electron wave packet from the  $z$  borders in Fig. 6(a) is expected to be stronger than that from the  $\rho$  border. The IIR's demonstrated in Fig. 7(a) are in agreement with this expectation. For each cycle of the laser pulse, there should be two distinct stages in the outgoing wave packet that passes alternatively from the two  $z$  borders, located respectively in the  $+z$  and  $-z$  directions. This is while the outgoing wave packet from the  $\rho$  border (red line) should be smooth, however still periodic (due to the periodic behavior of the pulse), with weak variations.

Figure 7(a) shows one baseline peak for the overall IIR and its  $z$  component for every half-cycle of the laser pulse related to the passage of the electron wave packet through the corresponding  $+z$  or  $-z$  borders. Intensity of this baseline peak reaches its maximum value over the first few cycles of the laser pulse. The first baseline peak is relatively weak. As can be seen from Fig. 7(a), the  $\rho$  component of the IIR for Fig. 6(a) setup of the simulation box shows always very weak variations and does not distinctly follow up the laser pulse shape. An outgoing electron from the  $z$  borders is strong as compared to that from the  $\rho$  border, which is weak. In this case, the total ionization rate can be considered to be mainly due to the ionization through the  $-z$  borders.

The  $+z$  and  $-z$  borders in Fig. 6(b) are placed at  $+50$  and  $-150$ , respectively. This situation of the  $-z$  borders results in two effects. First, the  $-z$  component IIR will be vanished for some initial half-cycles of the laser pulse due to the longer time needed for the electron wave packets to reach the  $-z$  border than to reach the  $+z$  border. Second, the intensity of the  $z$  component IIR corresponding to the outflow of electron

from the  $+z$  border at  $+50$  is very stronger than that of the  $-z$  border at  $-150$ , which is due to the fact that the  $+z$  border is closer to the center of the initial wave packet. These two effects result in the baseline peaks of the  $z$  component IIR with alternative intensities; the alternate strong positive peaks corresponding to the half-cycles in which the outflow is towards the  $+z$  direction and the alternative negative weak peaks corresponding to the half-cycles in which the outflow is towards the  $-z$  direction. A comparison between Figs. 7(a) and 7(b) shows that the outgoing electron from the  $+z$  border at  $+50$  overcomes the incoming electron from the  $-z$  border at  $-150$  when the electric field is in the  $+z$  direction, but the outgoing electron from the  $-z$  border at  $-150$  cannot overcome the incoming electron from the  $+z$  border at  $+50$  when the electric field is in the  $-z$  direction. Therefore, the negative and positive IIR peaks alternatively appear along each other in Fig. 7(b). It is only with this design of the simulation box, Fig. 6(b), that we can clearly observe the negative IIR. Figure 7(b) exhibits that the positive signals of the IIR (outgoing electron wave-packet signals) are strong and sharp but the negative signals of the IIR (returning electron wave-packet signals) are smooth and weak.

As the borders are moved sufficiently farther away from the nuclei [as in Fig. 6(c)], intensity of both positive and negative signals of the IIR becomes weaker at earlier time stages of the laser pulse, and probability of the returning electron wave packet (the negative IIR) becomes smaller, Fig. 7(c). Comparison of Figs. 7(b) and 7(c) shows that the negative IIR peaks are almost vanished for the simulation box of Fig. 6(c); only positive IIR peaks appear in Fig. 7(c). In addition, the positive peaks corresponding to the  $+z$  border become weaker in Fig. 7(c) as compared to those in Fig. 7(b). In Fig. 7(c), when the electric laser field is in the  $+z$  ( $-z$ ) direction, the outgoing electron from the  $+z$  ( $-z$ ) border overcomes the incoming electron from the  $-z$  ( $+z$ ) border. This, therefore, results in the IIR signals which are always positive.

To study the effect of the region boundary on the IIR signals and its components, we carried out two other sets of calculations based on the simulation boxes demonstrated in Figs. 6(d) and 6(e), which results are presented in Figs. 7(d) and 7(e), respectively. Comparison of Figs. 7(d) and 7(e) with Fig. 7(c) shows that for the present setup of the simulation box, positions of the box boundaries have insignificant effect on the IIR signals. The difference between Figs. 7(c)–7(e) can be interpreted based on the position of the boundaries according to the discussions presented above, i.e., the closer the borders to the center of the initial wave packet, the stronger the corresponding component IIR peaks. It is thus shown here that calculation of the IIR and its components is easily possible for any local area.

Figure 7 shows that the structure of the IIR peaks is determined mainly by its  $z$  component, and that the  $\rho$  IIR component has smooth structure. Furthermore, relative magnitudes of the IIR components depend strongly on the relative positions of the corresponding borders with respect to the center of the initial wave packet.

## VIII. CONCLUSION

We introduced and calculated exact component instantaneous ionization rates (IIR's) based on the instantaneous val-

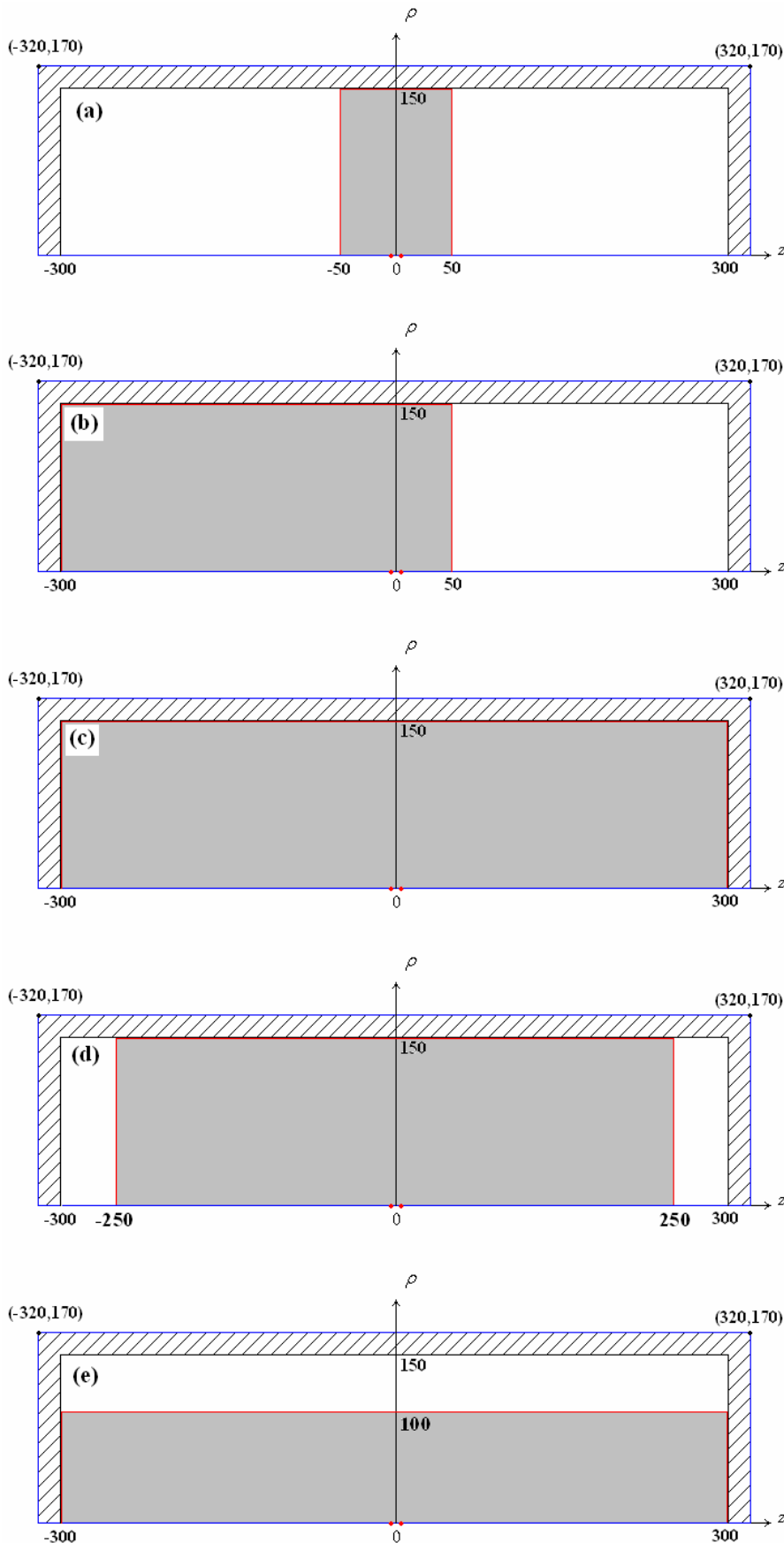


FIG. 6. (Color online) The different sub-boxes (highlighted in gray and bordered in red) designed for probing the evolution and ionization of the wavepacket of the electron in a simulation box of  $-300 \leq z \leq 300$  and  $0 \leq \rho \leq 150$ . The hatched strips show the absorber regions. The two (red) points near the origin represent the two H nuclei located symmetrically around the origin with a 9.6 distance in this case. These boxes span over (a)  $-50 \leq z \leq 50$ , (b)  $-300 \leq z \leq 50$ , (c)  $-300 \leq z \leq 300$ , and (d)  $-250 \leq z \leq 250$  all with  $0 \leq \rho \leq 150$ , and over (e)  $-300 \leq z \leq 300$  with  $0 \leq \rho \leq 100$ . The instantaneous ionization rates calculated for these sub-boxes are presented in Fig. 7.

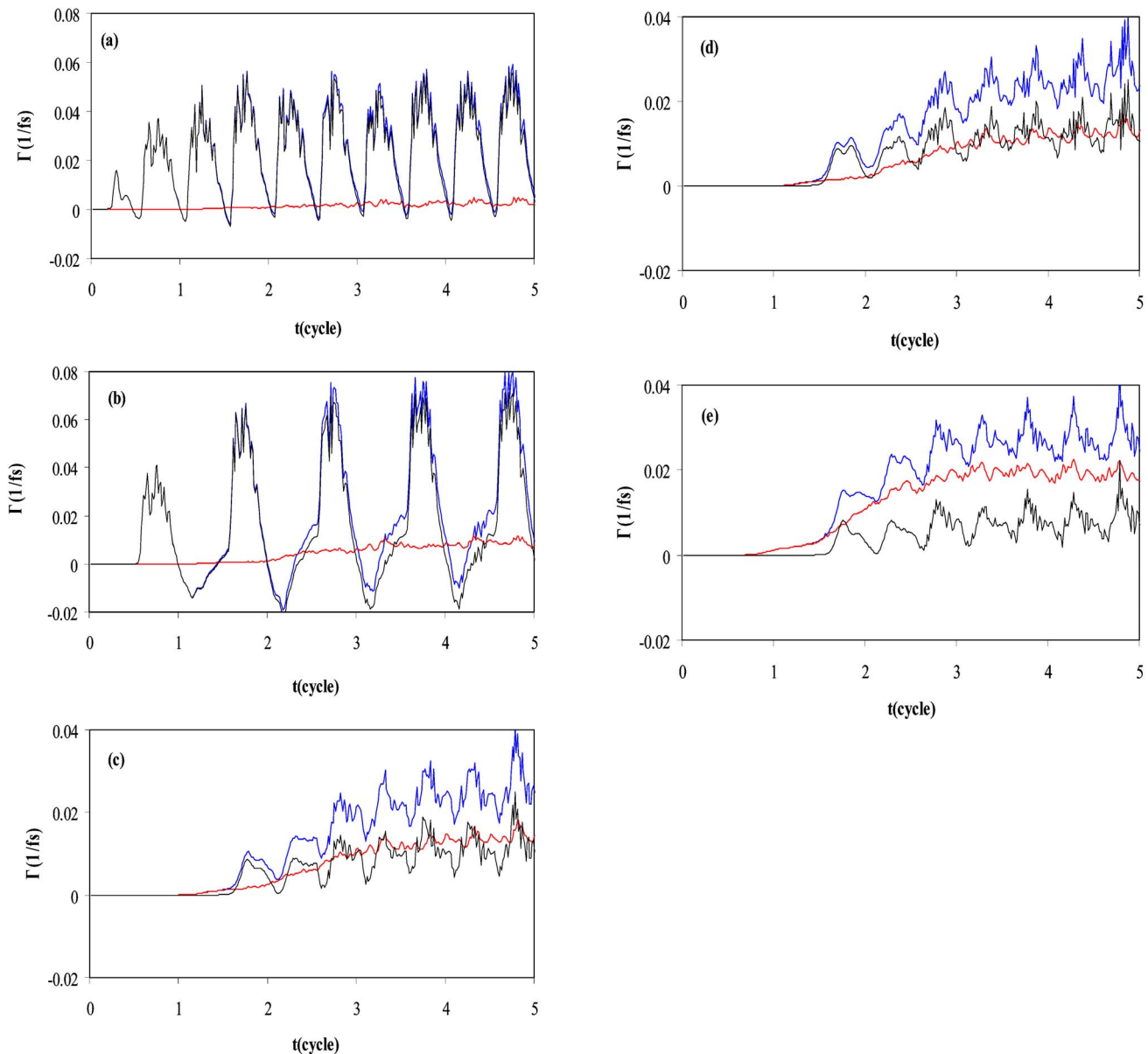


FIG. 7. (Color online) The instantaneous ionization rates corresponding to the sub-boxes introduced in Fig. 6. The simulations are carried out for  $R=9.6$  for the first five cycles of the linearly polarized laser pulse of  $I=1.0 \times 10^{14}$  W/cm<sup>2</sup> intensity and  $\lambda=1064$  nm wavelength which is turned on immediately as  $E_0 \cos(\omega t)$ , i.e., with  $f(t)=1$ . The IIR's (blue line) and their  $z$  (gray line) and  $\rho$  (red line) components correspond to the simulation boxes of Fig. 6.

ues of imaginary energy. We showed that the exact evaluation of the component (instantaneous) ionization rates is possible only with the calculation of component instantaneous imaginary energy and can be approximately calculated by the VD method. Moreover, details of the electron wave-packet evolution in different directions of the working space under the influence of the strong ultrashort laser field were studied by calculating components of the IIR. Analysis of the IIR signals and their components allows detecting and probing details of the behavior of the outgoing and incoming electron wave packets of the system in an intense laser field in attosecond time scale. In addition, it is also possible to follow the electron wave packet in the atomic unit space-time and to study details of the electron dynamics near the

nuclei [29]. It is shown that the positive signals of the component and overall IIR (outgoing electron wave-packet signals) are strong and sharp but the negative signals of the component and overall IIR (returning electron wave-packet signals) are smooth and weak.

It is revealed by the present results of the solution of TDSE that for H-H distances  $R < 5.6$ , when the laser pulse is turned on without a ramp, the first peak of the  $R$ -dependent ionization rates disappear and when the pulse of the laser field is turned on slowly (with a ramp), both lower and upper QES's contribute to construct the first peak of the ionization rates at  $R=4.8$ . For all of the  $R < 3.6$  and  $R > 5.2$  ranges, the ionization rates are determined by the lower QES, and the duration of the rising time of the laser pulse, i.e.,  $\tau_1$ , does not

have any significant effect on the contribution of the two QES's for the  $R < 3.6$  and  $R > 5.2$  ranges. Therefore, we show in this report that the TDSE and ac Floquet calculations together form a powerful tool to derive a detailed  $R$ -dependent structure of the ionization rates. The comparison between the results obtained by these two methods leads us to determine the individual contributions of the QES's to the overall ionization rates.

## ACKNOWLEDGMENTS

We would like to thank the University of Isfahan for financial support and research facilities. We should also acknowledge the Scientific Computing Center of the School of Mathematics, Institute for Studies in Theoretical Physics and Mathematics (IPM) of I. R. Iran for providing their high-performance computing cluster.

- 
- [1] M. Yu. Ivanov, A. Scrinzi, R. Kienberger, and D. M. Villeneuve, *J. Phys. B* **39**, R1 (2006).
  - [2] A. Giusti-Suzor, F. H. Mies, L. F. DiMauro, E. Charron, and B. Yang, *J. Phys. B* **28**, 309 (1995).
  - [3] *Molecules and Clusters in Intense Laser Field*, edited by J. Posthumus (Cambridge University Press, Cambridge, England, 2001).
  - [4] *Laser Control and Manipulation of Molecules*, edited by A. D. Bandrauk, Y. Fujimura, and R. J. Gordon (Amer. Chem. Soc. Symp. Series 821, Washington, DC, 2002).
  - [5] C. Cornaggia, J. Lavancier, D. Normand, J. Morellec, P. Agostini, J. P. Chambaret, and A. Antonetti, *Phys. Rev. A* **44**, 4499 (1991).
  - [6] D. Normand and M. Schmidt, *Phys. Rev. A* **53**, R1958 (1996).
  - [7] E. Constant, H. Stapelfeldt, and P. B. Corkum, *Phys. Rev. Lett.* **76**, 4140 (1996).
  - [8] K. Codling and L. J. Frasinski, *J. Phys. B* **26**, 783 (1993).
  - [9] T. Zuo and A. D. Bandrauk, *Phys. Rev. A* **52**, R2511 (1995).
  - [10] M. Schmidt, D. Normand, and C. Cornaggia, *Phys. Rev. A* **50**, 5037 (1994).
  - [11] J. H. Posthumus, L. J. Frasinski, A. J. Giles, and K. J. Codling, *J. Phys. B* **28**, L349 (1995).
  - [12] G. N. Gibson, M. Li, C. Guo, and J. Neira, *Phys. Rev. Lett.* **79**, 2022 (1997).
  - [13] I. D. Williams, P. McKenna, B. Srigengan, I. M. G. Johnston, W. A. Bryan, J. H. Sanderson, A. El-Zein, T. R. J. Goodworth, W. R. Newell, P. F. Taday, and A. J. Langley, *J. Phys. B* **33**, 2743 (2000).
  - [14] L. B. Madsen, M. Plummer, and J. F. McCann, *Phys. Rev. A* **58**, 456 (1998).
  - [15] Z. Mulyukov, M. Pont, and R. Shakeshaft, *Phys. Rev. A* **54**, 4299 (1996).
  - [16] A. D. Bandrauk and H. Z. Lu, *Phys. Rev. A* **62**, 053406 (2000).
  - [17] L.-Y. Peng, D. Dundas, J. F. McCann, K. T. Taylor, and I. D. Williams, *J. Phys. B* **36**, L295 (2003).
  - [18] M. Vafae and H. Sabzyan, *J. Phys. B* **37**, 4143 (2004).
  - [19] X. Chu and Shih-I. Chu, *Phys. Rev. A* **63**, 013414 (2000).
  - [20] M. Pont, D. Proulx, and R. Shakeshaft, *Phys. Rev. A* **44**, 4486 (1991).
  - [21] D. A. Telnov and Shih-I. Chu, *Phys. Rev. A* **71**, 013408 (2005).
  - [22] H. Sabzyan and M. Vafae, *Phys. Rev. A* **71**, 063404 (2005).
  - [23] D. Pavičić, A. Kiess, T. W. Hänsch, and H. Figger, *Phys. Rev. Lett.* **94**, 163002 (2005).
  - [24] Th. Ergler, A. Rudenko, B. Feuerstein, K. Zrost, C. D. Schröter, R. Moshhammer, and J. Ullrich, *Phys. Rev. Lett.* **95**, 093001 (2005).
  - [25] S. Chelkowski and A. D. Bandrauk, *J. Phys. B* **28**, L723 (1995).
  - [26] A. D. Bandrauk and H. Z. Lu, *J. Mol. Struct.: THEOCHEM* **547**, 97 (2001).
  - [27] G. L. Kamta and A. D. Bandrauk, *Phys. Rev. Lett.* **94**, 203003 (2005).
  - [28] M. Vafae, H. Sabzyan, Z. Vafae, and A. Katanforoush, <http://www.arxiv.org/abs/physics/0509072>
  - [29] M. Vafae (unpublished).